NUMERICAL SIMULATION OF LASER BEAM WELDING WITH DYNAMIC BEAM SHAPE SEQUENCING

C. DURÁN*,[1], C. ZENZ*, T. FLORIAN*, M. BUTTAZZONI*, A. OTTO*

**TU Wien, Institute of Production Engineering and Photonic Technologies, 1060, Vienna, Austria*
[1]Corresponding author

DOI 10.3217/978-3-99161-089-2-010, license CC BY 4.0

ABSTRACT

Dynamic beam shaping enables diverse possibilities to influence the performance of laser-based manufacturing processes, for example by tailoring the spatial intensity distribution of light in real time. One such possibility is shape sequencing, which involves switching between two or more beam shapes during laser-matter interaction, with each shape being active for a specified time frame (shape duration) within the sequence. When properly understood and utilized, shape sequencing could serve as an effective optimization approach in high-power laser materials processing applications such as Laser Beam Welding (LBW).

In this work, a multi-physical simulation model is used as a comprehensive framework to evaluate the impact of shape duration on the dynamics of the LBW process, with the aim of mitigating instabilities that can lead to defects such as pores, spatter, lack of penetration, cracks, etc. The long-term goal is not only to identify optimal welding parameters, but also to understand why certain shaping strategies lead to better or worse process outcomes. As a demonstration, an aluminum-magnesium alloy is chosen as the workpiece material for a deep penetration welding (DPW) scenario. The numerical model is initially validated by comparing simulation results with macrographs of experimentally produced welds and is subsequently used to analyze a welding setup incorporating dynamic beam shape sequencing. The study reveals that shape sequencing can effectively induce vibrations at predefined frequencies on the keyhole surface, manifesting as periodic pulses whose width is determined by the shape durations. This pulsed excitation is subsequently transmitted to the melt pool, influencing its behavior. Certain shape durations favor a more or less effective excitation of the melt pool.

Keywords: dynamic beam shaping, shape sequencing, shape duration, frequency analysis, multi-physical model

INTRODUCTION

In addition to adjusting process variables such as beam power, feed rate, weld path, or focus position, modulating the properties of the laser beam opens up an even wider range of parameter configurations that may help achieve targeted key performance indicators (KPIs) of the welding process. This approach, referred to as beam shaping, can be implemented by means of various methods and technologies. Schmidt et al. [1] categorize beam shaping into three types: spatial, temporal, and polarizational. Spatial beam shaping involves using shaping devices to produce a specific intensity and/or phase distribution at the workpiece after the beam propagates through free space. Temporal beam shaping refers to the modulation of the wave phase (instantaneous frequency) or amplitude (power) over time. Polarizational beam shaping modifies the polarization state of light using optical elements such as half-wave or quarter-wave plates. A central aspect highlighted in [1] is that, regardless of the beam shaping method or technology, the interaction between a moving laser beam and the material always results in dynamic energy coupling. Therefore, it is crucial that the laser beam interacts with the material within a suitable time frame that can meaningfully influence the welding process or any of its mutually dependent subprocesses.

From a technological perspective, the spatial, temporal, or polarization properties of light can be modulated in an initial step and then remain constant throughout material processing, which is commonly referred to as static beam shaping. However, they can also be modulated "on the fly" and repeatedly during processing, which is referred to here as dynamic beam shaping. This work explores dynamic beam shaping based on Civan's coherent beam combining (CBC) proprietary technology [2], which enables both spatial and temporal modulation of light. For CBC beams, Weber et al. [3] proposed an additional classification by comparing the "relevant time" of the process (or subprocess), referred to therein as the process time constant, with the time(s) determined by the motion of the heat source. In this context, the laser-matter interaction regime is considered quasi-static when the beam moves faster than the response time of a particular physical process, causing the material to experience a temporally and spatially averaged influence of the heat source; dynamic when the beam motion occurs over a time significantly longer than the relevant process timescale; and resonant when the beam motion occurs over a time approximately equal to the characteristic process time.

Building on this, a reasonable follow-up step is to identify the characteristic timescales or frequencies of the subprocesses in LBW and to determine how this information can guide the selection of beam shaping parameters that effectively operate on one or more of these subprocesses to achieve improved welding results. Depending on the technology, beam shaping can involve several independently adjustable parameters, i.e., multiple degrees of freedom, that define the behavior of the laser heat source and, therefore, the process outcome. While this offers great versatility, the complexity of the highly dynamic and interdependent physical interactions during welding makes it difficult to recognize the precise role of each individual shaping parameter in the mechanisms governing weld attributes.

For Civan's CBC technology, experimental studies have been recently conducted to evaluate the impact of different shaping parameters on the welding process. Dittrich et al. [4] performed bead-on-plate (BoP) welding tests on oxide-free copper using 18 beam shapes with

shape frequencies between 0.1 and 300 kHz, at a fixed power and feed rate of 6 kW and 6 m min^{-1}, respectively. It was observed that, in the considered process window, simpler shapes such as spots, short lines or small rings, produced better weld quality at different frequencies than larger and more complex shapes. Sawannia et al. [5] investigated the influence of switching frequency (shape duration) when sequencing between a single spot and four spots during welding of AISI 304 stainless steel plates (5 mm thickness), at a welding speed of 6 m min^{-1} and power of 5 kW. They tested switching frequencies of 0.01, 0.1, 1, and 10 kHz (corresponding to shape durations of 100, 10, 1, and 0.1 ms, respectively) and identified a clear process response to shape sequencing for durations larger than 10 ms. Prieto et al. [6] analyzed the influence of beam shape, feed rate, and shape frequency on overlap welding of 0.8-mm-thick AA3003 aluminum alloy sheets using input powers between 2.4 and 3.6 kW. They found that infinity and spiral shape patterns yielded satisfactory results in terms of interface width, penetration, and interface defects when using shape frequencies above 10 kHz at feed rates up to 18 m min^{-1}. Olschok et al. [7] carried out BoP tests on 8-mm-thick AH36 steel at a speed of 1.2 m min^{-1}. A single-point fixed pattern and three dynamic shapes at frequencies of 0.1 and 100 kHz were tested, all achieving full penetration with powers between 10 and 13 kW. The authors reported that shape frequency strongly influenced the melt pool geometry and resulting weld bead. At 100 kHz, the melt pool became narrower and longer. At 0.1 kHz, the welds produced by the dynamic shapes were similar in geometry and microstructure to the weld produced by the single-point pattern, whereas at 100 kHz, the cross sections showed a markedly different geometry and coarser grains.

Although an impact of dynamic beam shaping on the LBW process can be demonstrated experimentally, as in the examples above, deeper understanding of the specific effects of individual parameters is difficult to obtain through experimentation alone. In this regard, numerical simulation becomes an essential tool for advancing knowledge about the capabilities of different beam shaping strategies with respect to welding process optimization. As an application example, this work investigates one specific shaping parameter from Civan's CBC technology: the switching frequency (or shape duration) during sequencing of two shapes. Numerical simulations using the multiphase Mass-of-Fluid model described in [8] are conducted to gain insights into the effect of this parameter on the welding process. A 5xxx series aluminum-magnesium alloy is selected for the study, focusing on full penetration welds in a BoP configuration with 6 mm thick plates. This alloy series is widely used in aerospace, transportation, and construction owing to their low density, cost-effectiveness, high specific strength, good ductility and toughness, and excellent machinability, weldability, and corrosion resistance [9]. Defects such as pores and cracks are among the main challenges in LBW of such alloys [10].

The first part of this work provides a brief description of the numerical model, with an emphasis on the simulation aspects relevant to this practical application. It includes an overview of the laser heat source and its technology-specific shaping parameters. To ensure the simulation study is conducted within a sufficiently robust numerical framework, the model is validated by comparing simulation results with macrographic cross-section images for two significantly different parameter sets. Using the validated model, sequencing with beam shapes symmetrical about the process mid-plane is simulated with different symmetrical-in-time durations, i.e., identical durations for each shape, to evaluate the effect of this single

parameter on the welding process. The results are presented and discussed in the final part of the document, with the aim of identifying and explaining the main effects of shape duration and the specific shaping strategy on the process outcome, as well as their potential relationship with system dynamics.

NUMERICAL MODEL AND SIMULATION SETUP

The selected beam shaping strategy was investigated through one-pass BoP welding simulations of 5083 aluminum-magnesium alloy, employing a multi-physical numerical model custom-built within the OpenFOAM® architecture (Open Field Operation and Manipulation) [11], where the systems of coupled partial differential equations are solved via the Finite Volume Method (FVM). Originally introduced over a decade ago [12-13], the model has since been turned into a universal framework capable of simulating various scenarios of laser-based manufacturing both in the domains of micro- and macro-processing [14]. Fig. 1 exemplarily shows one of the deep penetration welding (DPW) processes simulated within this study, highlighting some of the key features captured by the simulation model.

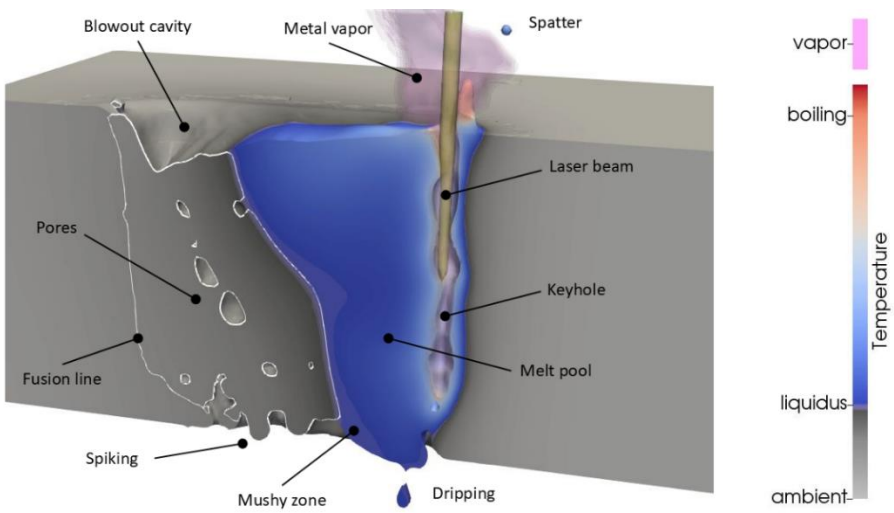

Fig. 1 Longitudinal clip of the simulated LBW process in a 9 mm-thick 5083 aluminum plate

The model itself was recently described in detail and rigorously validated by Zenz et al. [8]; hence, the reader is referred to [8] for a comprehensive list of underlying assumptions, governing equations, numerical implementation details, and validation results for different materials and process regimes relevant to laser beam welding. Instead of the widely used Volume-of-Fluid (VoF) method, it employs the so-called Mass-of-Fluid (MoF) method, in which the mass and energy of each phase are directly tracked through conservation equations,

yielding an inherently mass- and energy-conservative framework, even across phase-change events and throughout compressible scenarios.

Gaseous phases are included in the modeling domain and, in contrast to virtually all other published models, evaporation and condensation rates are formulated as pressure-dependent, with the local pressure on the gaseous side of the liquid-vapor interface taken into account to yield accurate, dynamic rates of evaporation and condensation. Furthermore, the recoil pressure resulting from newly formed and expanding vapor acting on condensed matter is a direct result of the compressible multiphase formulation including gaseous matter; hence, as opposed to most published approaches, no simplified recoil pressure model is necessary.

Consequently, the MoF-based framework offers strong predictive capabilities for highly dynamic events in laser-material processing, with no need for calibration to a specific scenario (unlike models that neglect pressure-dependent evaporation and condensation), as recently demonstrated by Zenz et al. [15]. On this basis, it is particularly well-suited to reproduce and analyze transient system behavior and the resulting process characteristics under temporally and spatially modulated laser intensity distributions, including the low- and high-frequency response of the system to such modulation. By accounting for local gas-side pressure variations and their dependence on laser irradiation, as well as the topological constraints affecting the transport of newly formed vapor out of the laser irradiation zone, no process-, time- or space-dependent evaporation efficiency is required to capture the resulting non-equilibrium state of evaporation and condensation. Further details and a rigorous comparison of the compressible multiphase MoF model with a simulation model omitting pressure dependence in evaporation and condensation are provided in [15].

While the underlying physics are formulated in a general manner and are universally applicable to many laser-based manufacturing processes, the model requires material properties, process parameters, geometry, and initial and boundary conditions as inputs, just as in real-life applications. The following subsections focus on these parameters.

General aspects of the simulation setup

For the BoP welding configuration, Fig. 2 shows a schematic of the computational domain, which consists of the 5083-alloy workpiece and upper and lower layers of still air at 1 atm as the surrounding gas. Appendix I lists the temperature-dependent material properties used in the simulations for both the aluminum–magnesium alloy and air. Where no literature data were available for the specific alloy, values for pure aluminum were assumed.

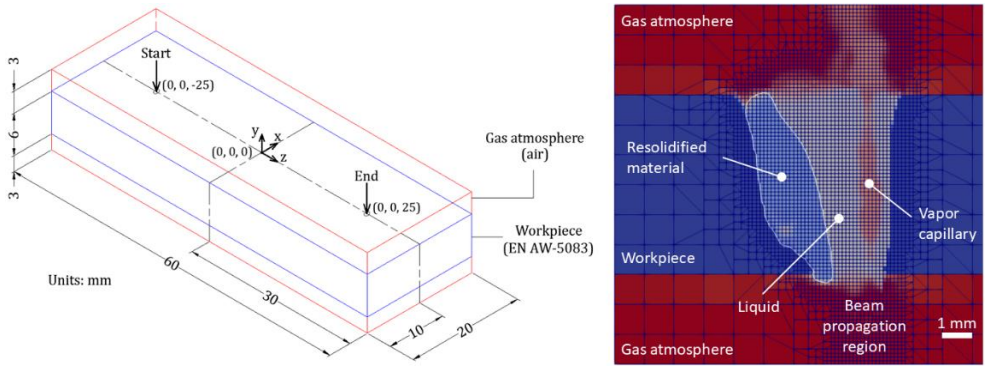

Fig. 2 Dimensions of the computational domain (left) and mesh (right), with refinement in regions corresponding to beam propagation, liquid, and resolidified material phases

The initial mesh comprises cubic cells of 1 mm side length, distributed uniformly across the computational domain. Dynamic mesh refinement is employed, with a maximum of three refinement levels, resulting in the smallest cell elements having a side length of 125 µm. A portion of the mesh longitudinal section is also included in Fig. 2. The computational time step was adapted according to the Courant–Friedrichs–Lewy (CFL) condition, with a maximum value limited to 0.5 in the present simulations. An upper bound of 3 µs was further imposed on the time step, selected based on the lifetime of a single CBC point of the dynamic shapes employed (see Table 1 in next section). The workpiece boundaries were set to a fixed velocity of (0, 0, 0) and a zero-gradient condition for temperature, while the atmosphere boundaries were assigned a zero-gradient condition for velocity and an inlet/outlet condition for temperature.

In the computational domain, the coordinate system is located at the top of the workpiece. The arrows indicate the start and end positions of the laser's linear path, with the beam oriented perpendicular to the workpiece. The geometry was chosen to be sufficiently large to allow the process to reach a quasi-steady state. An important aspect of the chosen geometry is that no process symmetry is assumed, i.e., the entire weld bead is simulated. This allows, on one hand, modelling the specific shaping strategy analyzed, namely side-by-side shape sequencing, and, on the other hand, capturing asymmetric phenomena, such as the alternating lateral movement of the melt pool, that would be missed if symmetry conditions were assumed.

HEAT SOURCE AND PROCESS PARAMETERS

Beam shaping is applied using Civan's Dynamic Beam Laser (DBL), which integrates Coherent Beam Combining (CBC) and Optical Phased Array (OPA) technologies. CBC takes a seed laser input, splits it, and amplifies it in parallel across multiple channels before recombining them coherently to produce a single high-power, high-quality beam. OPA controls the phase of each element in a 2D array, allowing the output beam to be shaped and steered arbitrarily without moving parts. Together, CBC maximizes power, while OPA

provides precise control over beam shape and direction [2]. The principle of operation of the DBL, as well as a detailed description of the shaping parameters, can be found in [3]. The beam shapes used in this study are shown in Fig. 3.

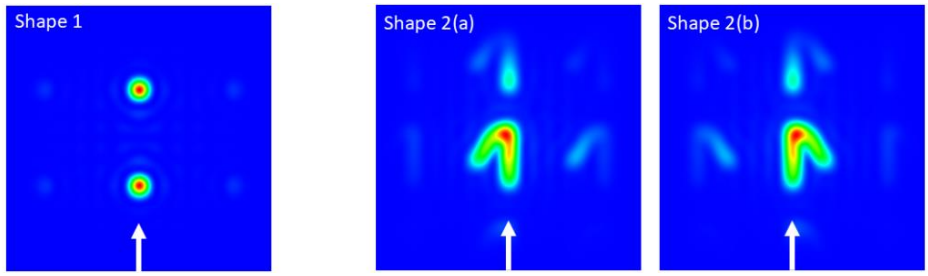

Fig. 3 Dynamic beam shapes: Shape 1 comprises 2 CBC-points; Shapes 2(a) and 2(b), 22-CBC points each. The white arrow aligns with the weld mid-plane and indicates the feed direction

Each beam shape consists of a sequence of individual CBC points, with only one point active at a time during a shape cycle. Consequently, the patterns observed in Fig. 3 represent the superposition of the focal intensity distributions of all CBC points composing the shape, assuming an infinitely high shape frequency ($f_{SR} \to \infty$). For this study, a main-lobe focal diameter of 85 µm (FWHM) was used, corresponding to a focal length of 1.5 m and a depth of focus of 11.5 mm at a laser wavelength of 1064 nm. At this focal length, the CBC point can cover an area up to 520 µm wide. The main lobe is defined as a single spot at the center of the laser active area. In the numerical model, each CBC point is implemented as a series of two-dimensional arrays describing the intensity distribution at different planes along the propagation direction. Values at out-of-plane positions are linearly interpolated between the two nearest adjacent planes.

Table 1 summarizes the main shaping parameters, following the nomenclature presented in [3], while Table 2 lists the process parameters used for numerical validation (simulations 1a and 1b, based on experiments by Civan) and for examining different switching frequencies when sequencing between Shapes 2(a) and 2(b) (simulations 2a, 2b, and 2c).

Table 1 Shape parameters

Shape parameter	Symbol	Shape 1	Shapes 2(a) and 2(b)
Total number of positions in the shape	N_{Pos}	2	22
Number of set points at the *i*-th position	$N_{C,i}$	1	1
Total number of points in the shape	$N_{SP} = \sum_{i=1}^{N_{Pos}} N_{C,i}$	2	22
Shape refresh frequency	f_{SR}	10 kHz	15 kHz
Point order followed within the shape	-	-	Random
Time for drawing the complete shape	$t_{SR} = 1/f_{SR}$	100.0 µs	66.67 µs
Lifetime of one single CBC point	$t_{SP} = t_{SR}/N_{SP}$	50.0 µs	3.03 µs

Table 2 Process parameter sets

Parameter	1a	1b	2a, 2b, 2c
Plate thickness	6 mm	9 mm	6 mm
Power	5.5 kW	9.2 kW	5.5 KW
Feed rate	35 mm s^{-1}	60 mm s^{-1}	35 mm s^{-1}
Shape sequencing	No	Yes	Yes
Shapes employed	Shape 1	Shape 2(a) Shape 2(b)	Shape 2(a) Shape 2(b)
Shape duration in sequence (switching frequency) †	-	10 ms (100 Hz)	**2a:** 5 ms (200Hz) **2b:** 10 ms (100 Hz) **2c:** 15 ms (66.67 Hz)

† The same shape duration applies to Shape 2(a) and Shape 2(b).

RESULTS AND DISCUSSION

MODEL VALIDATION

A validation procedure was carried out to ensure that the simulations generated sound numerical results and adequately reflected the process under study, even when performed with widely different parameter sets, namely 1a and 1b. Fig. 4 shows a comparison between the simulation results and experimentally obtained macrographs of the weld cross-sections.

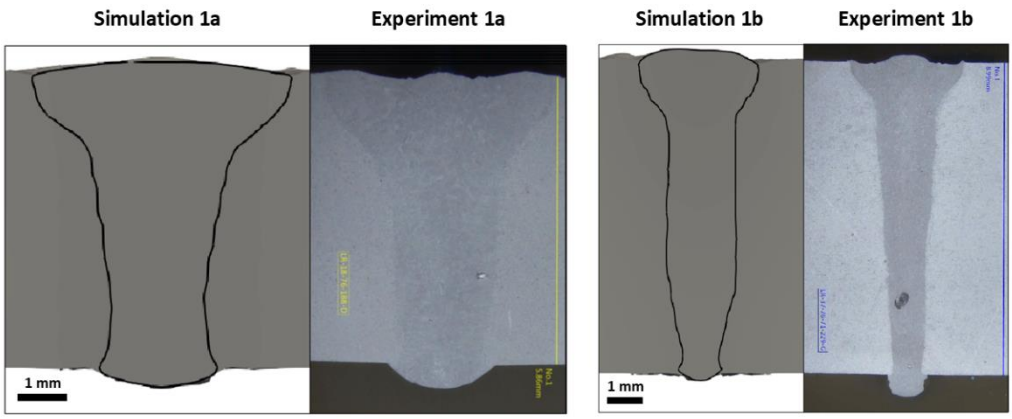

Fig. 4 Comparison between simulation and experimental results for parameter sets 1a (left) and 1b (right), using cross-sections representative of the process

Despite uncertainties in the material properties, particularly at high temperatures in the liquid state, the simulation results show good agreement with the experimentally obtained

cross-sections. Accuracy can be further improved by increasing the mesh resolution, reviewing the interpolation methods for describing the beam intensity, or performing additional iterations in the identification of thermophysical properties.

For the 9 mm plate, a larger difference is observed between simulation and experiment, mainly in the lower part of the weld bead, where the simulation predicts a wider bead due to more heat reaching the plate's lower section. This discrepancy could be related to a simplified description of the beam intensity distribution along the propagation direction. Although the numerical model is capable of a full three-dimensional description of the caustic, the simulations assumed a constant beam diameter along the plate height, given a depth of focus of 11.5 mm. This simplification appears reasonable for the 6 mm plate, which is the main focus of this study. However, for the 9 mm plate, beam divergence near the lower section can reduce the actual heat input, resulting in a narrower weld.

WELDING PROCESS EVALUATION

The evaluation of the welding process starts by comparing the influence of the beam shaping parameters on the geometry of the melt pool (~10 mm in length). As shown in Fig. 5, the overall dimensions and shape of the melt pool are very similar across all parameter sets for the 6 mm plate. This is consistent with the fact that the linear heat input (power-to-velocity ratio) is the same for all cases. Furthermore, the lateral asymmetry introduced by the sequencing strategy applied is subtle, since most of the intensity of the half-arrow (see Shapes 2(a) and 2(b) in Fig. 3) is concentrated at the process mid-plane.

Certain features can be identified in the velocity fields included in Fig. 5, which presents exemplary results from Simulation 1a for a plane perpendicular to the laser beam (0.5 mm below the workpiece top surface) and a longitudinal section of the process. In the former, vortices can be observed on each side of the keyhole region, located in the widest part of the melt pool. A high-turbulence region also develops near the necking zone at the rear part of the pool. In the longitudinal view, a clear clockwise recirculation pattern is visible. Despite evolving differently over time, similar flow structures were observed for the parameter sets in which shape sequencing was applied.

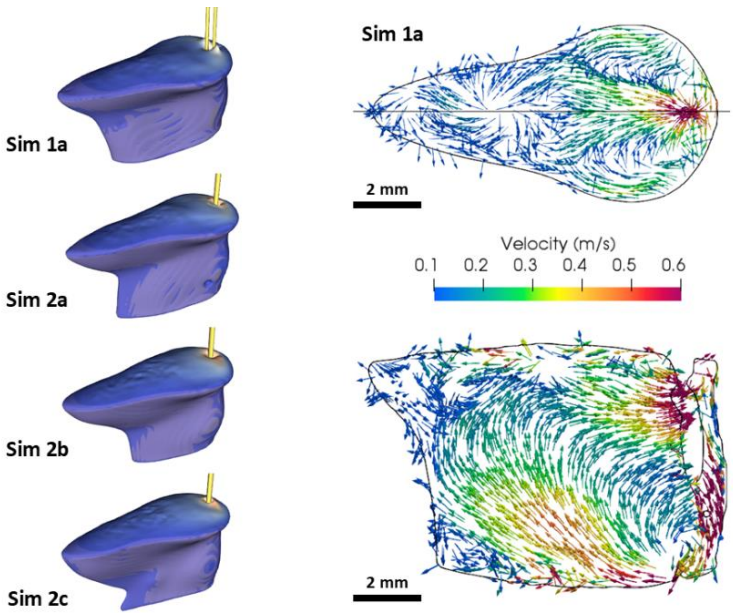

Fig. 5 Three-dimensional melt pool geometry (left), velocity vectors on a plane perpendicular to the beam (top right), and on the mid-plane (bottom right)

Selected process indicators, including the occurrence of spatter, dripping events, porosity, and keyhole closure events, were examined, and the results are summarized in Fig. 6. For spatter and drips, event monitoring was performed during the simulation with a sampling frequency of at least 333 kHz (corresponding to a computational time step of less than 3 μs), providing very high sensitivity. Only 'macro' droplets with a volume equivalent to that of a sphere with a diameter of minimum 0.15 mm, were considered, as in [16]. Keyhole full closure events were identified based on keyhole aperture measurements at the process mid-plane, 0.5 mm below the workpiece surface. The latter was done in a postprocessing phase, using a sampling frequency of 2 kHz. Porosity was also estimated during postprocessing as the fraction of the bead volume occupied by pores.

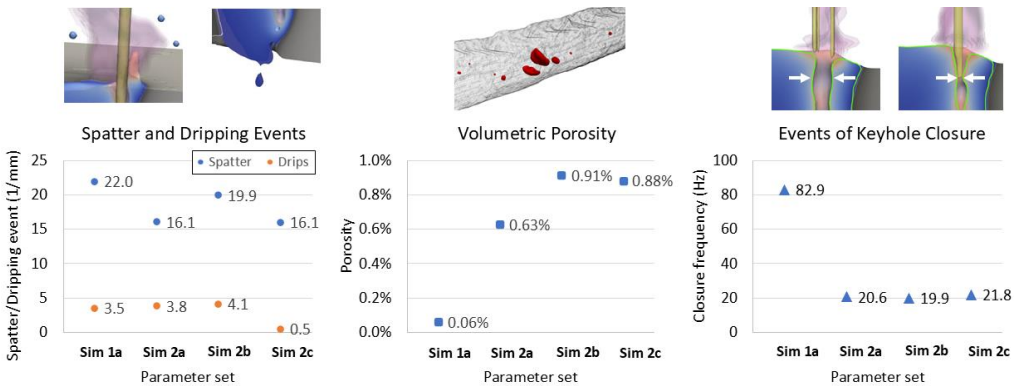

Fig. 6 Assessment of spatter, dripping, porosity, and keyhole closure

Measurements indicate spatter rates of 16.1-22.0 events per mm of weld (563-770 Hz), while dripping remains lower at 3.5-4.1 events per mm (122-143 Hz), except in Sim 2c, where it was significantly reduced. Among parameter sets 2a to 2c, a shape duration of 10 ms produced the highest spatter rate. Volumetric porosity was lowest for parameter set 1a (2-point shape), at about one-tenth of the porosity obtained for the other parameter sets, where side-by-side sequencing was used. The latter is an important indicator of potential instabilities in the welding process, resulting from the specific shaping strategy and parameters employed. Typical pores for the sequenced shapes at durations of 5, 10, and 15 ms are shown in Fig. 7.

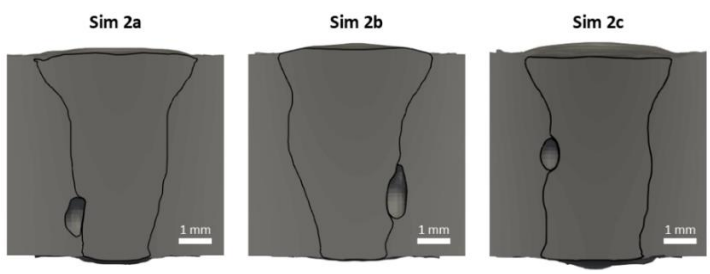

Fig. 7 Fusion line pores from non-optimal shape durations in side-by-side sequencing

Note the pronounced asymmetry in the bead cross section for the 10 ms shape duration (Sim 2b). This asymmetry appears to promote the formation of a relatively large pore on the opposite side. A comparable, though weaker, effect is observed in the other two cross sections. The pores share similar characteristics, being enlarged and located along the fusion line.

The average keyhole aperture and its standard deviation were estimated as 590 ± 196 µm, 454 ± 155 µm, 418 ± 136 µm, and 449 ± 166 µm for parameter sets 1a, 2a, 2b, and 2c, respectively. These values correspond closely to the maximum displacement of the CBC point for each specific shape pattern, as shown in Fig. 3, where Shape 1 spans a larger distance in the feed direction than Shapes 2(a) or 2(b). Keyhole closure events were observed at a frequency of about 20 Hz for parameter sets 2a to 2c, and about 83 Hz for parameter set 1a.

This relatively large difference can be explained by the behavior of the keyhole along the propagation direction. The leftmost part of Fig. 8 illustrates this, showing a longitudinal clip of the keyhole for both shaping configurations. In the case of the 2-point shape, the measurement routine (due to the way it was implemented) captured not only full keyhole closures but also partial closures, where the path of the rear high-intensity beam is interrupted by molten metal while the leading high-intensity beam continues through the keyhole. The tool for measuring keyhole closure did not account for this specific behavior of the 2-point shape. This situation does not occur with the half-arrow shapes, where only one high-intensity beam is present at a time, accompanied by one or more weaker side maxima depending on the position of the CBC point. When the path of the single high-intensity spot is interrupted, a full closure is very likely to occur.

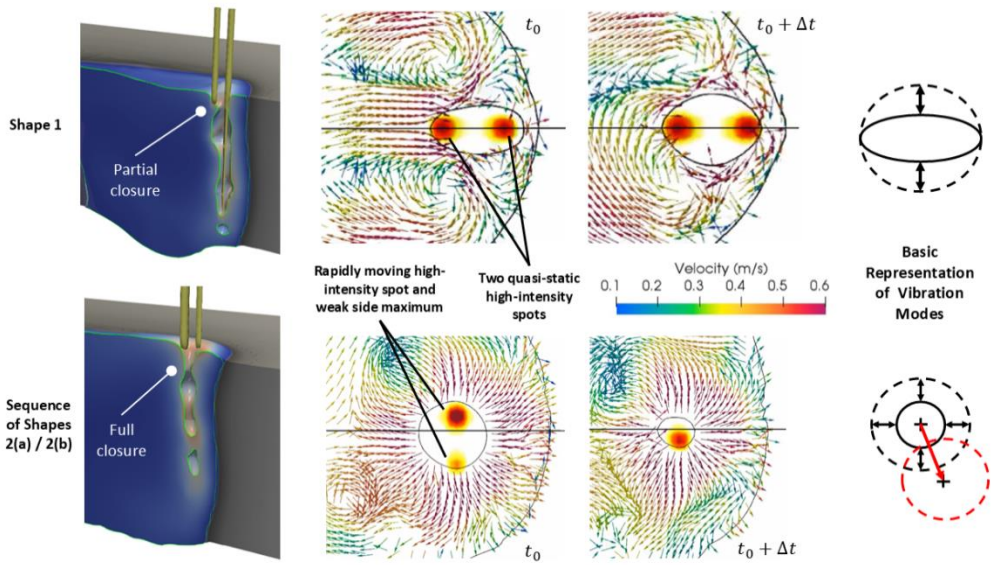

Fig. 8 Keyhole behavior and vibration modes on a plane perpendicular to beam propagation. The vectors represent the velocity field in the melt pool.

Another interesting observation arises from the behavior of the keyhole in a plane perpendicular to the beam, as shown in the central part of Fig. 8. The keyhole produced by the 2-point shape shows marked differences from that generated by switching between the two half-arrows, in terms of both geometry and vibrational modes, as schematized in the rightmost part of Fig. 8. The modes shown are the most prominent, identified through visual inspection of postprocessed high-resolution simulation videos. The 2-point configuration exhibits a dominant vibration in the transverse direction relative to the feed, where the two high-intensity beams, separated by a constant distance throughout the process, effectively lock the vibration mode in this transverse direction. By contrast, sequencing between two half-arrows results in

a radial vibrational mode, combined with a slight displacement of the keyhole center (exaggerated in Fig. 8), leading to a swaying motion of the keyhole surface.

These findings point to the first important insight: the keyhole exhibits different vibration modes depending on the beam shape and shaping strategy. Therefore, each shaping configuration should be analyzed with respect to its specific vibration modes. In the next subsection, the process dynamics are examined in greater detail.

INFLUENCE OF SHAPING STRATEGY ON THE WELDING PROCESS

Based on the observed vibrational modes for the shaping configuration with side-by-side sequencing, two sampling points were selected along the process longitudinal plane to monitor the local velocities during welding: $\boldsymbol{v_k}$ at the keyhole wall and $\boldsymbol{v_m}$ at the upper free surface of the melt pool, as shown in Fig. 9. These measurements were used to evaluate how the system responds to different shaping configurations, namely parameter sets 1, 2a, 2b, and 2c. The probe for $\boldsymbol{v_k}$ is at the rear part of the keyhole surface, located 0.5 mm below the workpiece surface, while the probe for $\boldsymbol{v_m}$ is located at the melt free surface, 2 mm behind the moving laser. The velocity measurement was performed at each computational step of the simulation, corresponding to a minimum sampling frequency of 333 kHz.

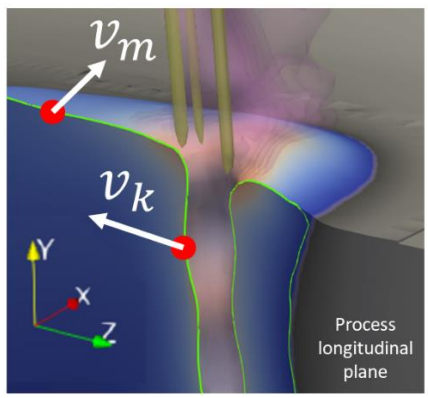

Fig. 9 Selected probe locations for velocity measurement

After reviewing the different velocity signals obtained at the keyhole, the transverse component with respect to the feed direction, $v_{k,x}$, reveals a particularly interesting behavior, as shown in Fig. 10. When sequencing with two shapes symmetric about the process mid-plane, as in this work, the excitation induced by beam shaping manifests as a pulsed pattern at the keyhole wall, acting in the transverse direction to the feed. The pulse period corresponds to a full sequencing cycle, i.e., the sum of the two shape durations. This is demonstrated in Fig. 10 for all simulations where sequencing was applied. Parameter set 1a, which represents a process-symmetric shape without sequencing, is included for reference.

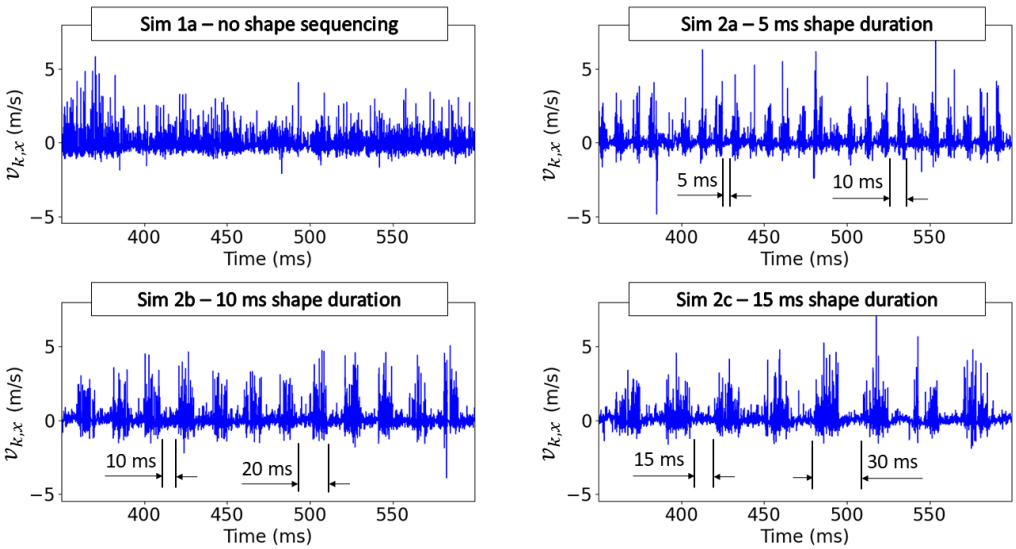

Fig. 10 Transverse component of the velocity signal at the keyhole, $v_{k,x}$

The nature of the pulses can be understood from the specific beam-shaping strategy applied, exemplified in Fig. 11 with a shape duration of 10 ms.

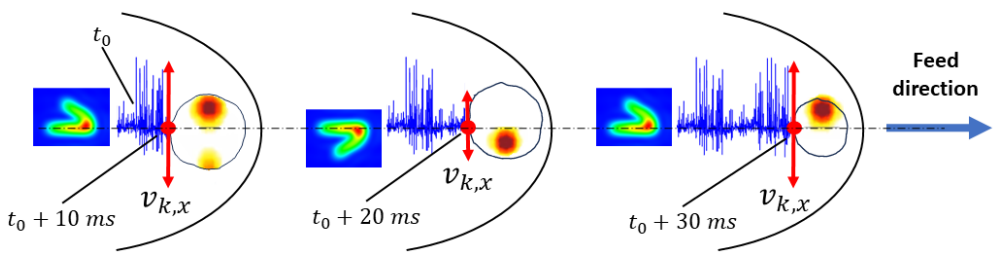

Fig. 11 Transverse component of the velocity signal at the keyhole, $v_{k,x}$

At time $t = t_0$, the sampling point at the back of the keyhole, initially vibrating at low amplitude, is instantaneously excited by Shape 2(a), inducing a high-amplitude vibration during 10 ms (pulse width). When switching to Shape 2(b), this vibration is effectively cancelled by the opposite excitation, resulting in a relatively calm signal for the next 10 ms. The cycle then repeats. In this case, a complete cycle lasts 20 ms (10 ms + 10 ms), corresponding to a frequency of 50 Hz. For symmetric-in-time sequencing with individual shape durations of 5 and 15 ms, the cycle periods are 10 ms and 30 ms, corresponding to frequencies of 100 Hz and 33.3 Hz, respectively.

The velocity signals from the keyhole wall were further analyzed in the frequency domain using Welch's method [17] to estimate the Power Spectral Density (PSD), which shows the frequencies at which most of the vibration energy is concentrated, making it a useful

complement to the Fast Fourier Transform (FFT) in the identification of dominant frequencies. The results are shown in Fig. 12, where, for each parameter set, both a low-frequency analysis (up to 200 Hz) and a high-frequency analysis (up to 5 kHz) were performed.

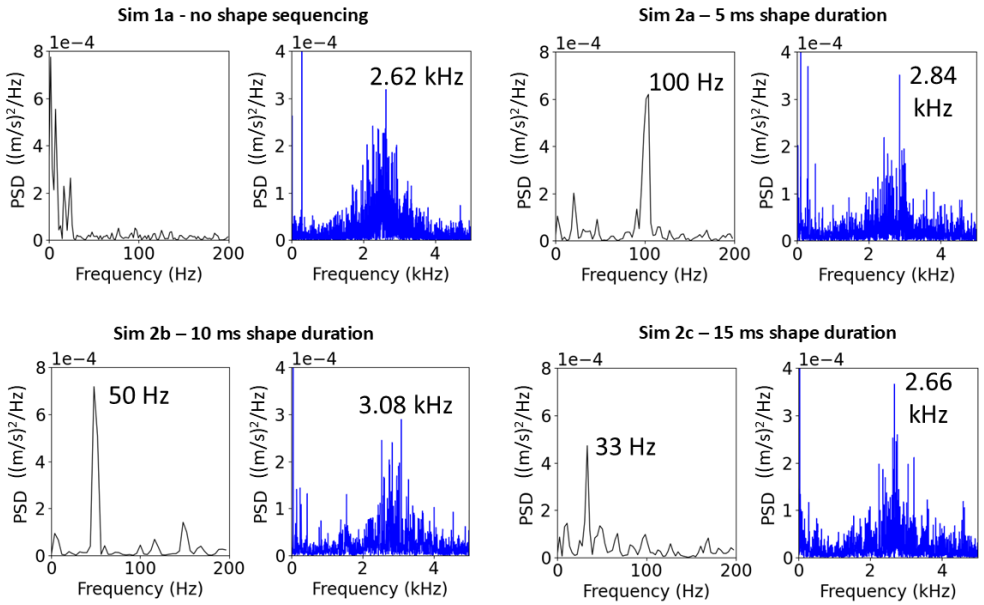

Fig. 12 PSD analysis for $v_{k,x}$

In the low-frequency domain, the PSD clearly shows that the frequency corresponding to one complete sequencing cycle, i.e., the sum of the shape durations, is directly mirrored at the keyhole surface. This is a remarkable insight, as it demonstrates that the excitation frequency of the keyhole (at least in its upper region) can be directly controlled by adjusting a simple shaping parameter, namely the shape duration. In the high-frequency domain, a very similar frequency appears across all parameter sets, including the one without shape sequencing. This frequency, in the range of 2.5 to 3.5 kHz, is most likely related to local surface modes corresponding to small-scale vibrations of the membrane forming the keyhole wall. Such modes could be excited, e.g., by proper selection of the shape refresh frequency, f_{SR}.

The velocity signals at the melt pool free surface and the corresponding frequency analyses are shown in Figs. 13 and 14, respectively. The selected sampling point exhibits a velocity amplitude nearly an order of magnitude lower than that observed at the keyhole. Reduced fluctuations around zero are observed for the sequenced configurations compared to parameter set 1a. In the high-frequency domain (up to 2 kHz), frequencies in the range of 300-500 Hz draw attention. These may correspond to damped oscillations originating from the periodic opening and closing of the keyhole (radial vibration mode) at a higher frequency. A more detailed and precise analysis is required for this specific vibration mode, as well as for the

lateral displacement of the keyhole center, i.e., the swaying or meandering effect illustrated in Fig. 8.

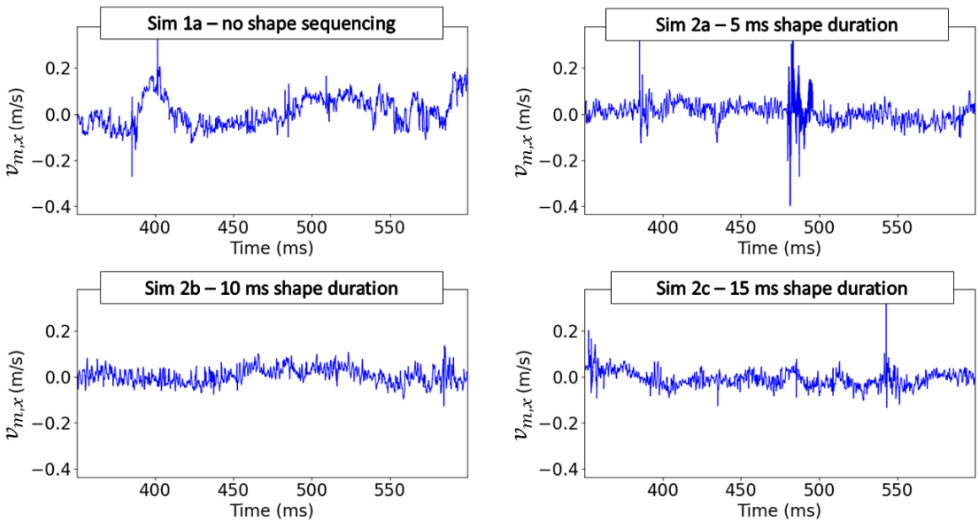

Fig. 13 Transverse component of the velocity signal at the melt pool upper free surface, $v_{m,x}$

From the measurements at the melt pool, the most notable observation arises in the low-frequency PSD plots in Fig. 14, where the full-cycle sequencing frequencies for symmetric shape durations of 10 and 15 ms (corresponding to 50 and 33.3 Hz, respectively) are clearly identifiable, with the 33 Hz peak being more pronounced than the 50 Hz peak. For parameter set 2a, with a 5 ms shape duration, a peak at 100 Hz is also present, but very weak. The PSD plots for this shape duration show qualitatively similar behavior to that of the reference case without shape sequencing.

The latter suggests two things. First, the mechanical lateral vibrations induced by the laser beam on the keyhole (by means of side-by-side shape sequencing) are successfully transmitted through the melt pool, as observed at a point on its free surface, 2 mm behind the heat source. Second, the excitation produced by certain shape durations is transmitted with higher energy, making these durations more effective in stimulating the vibrating system.

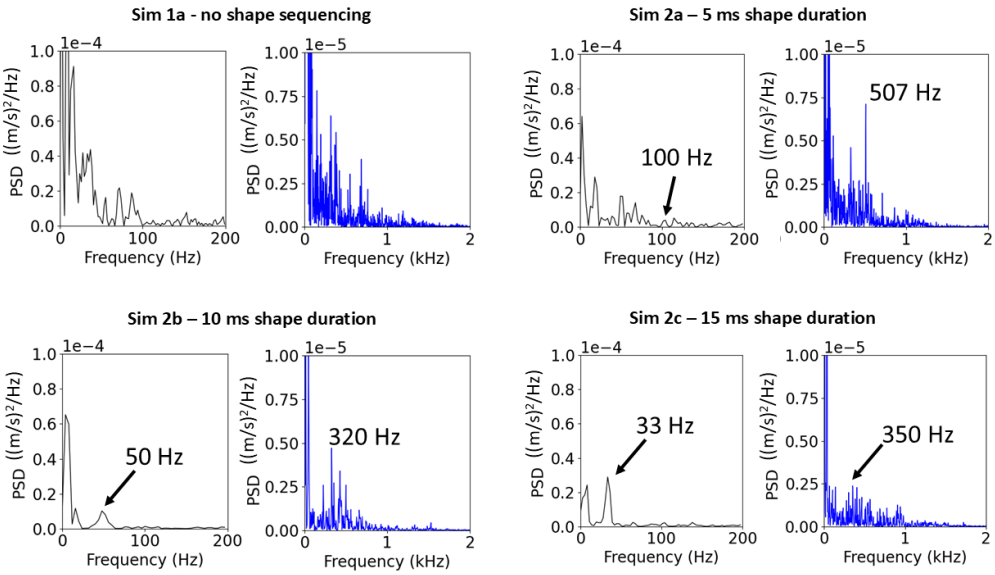

Fig. 14 PSD analysis for $v_{m,x}$

The beam shapes and shape durations chosen for the applied sequencing strategy clearly influence the process, with some having a stronger effect than others. In this case, since the system could not be properly dynamically balanced, the examined configurations resulted in unsatisfactory welding outcomes, including pores or pronounced asymmetries in the cross section, as shown in the weld characterization presented in the first part of this study. There may exist a specific switching frequency (or multiple frequencies) that yields improved weld quality. The initial idea behind sequencing Shapes 2(a) and 2(b) was to introduce a subtle asymmetry in the process, small enough to preserve overall weld symmetry, yet sufficient to excite the melt pool and influence the temperature gradients that govern, e.g., grain growth during solidification, thereby helping to mitigate defects such as pores or mid-line cracks. However, achieving this effect requires identifying the optimal shape duration(s).

One possible approach is to excite a process subsystem at its resonant frequency. Work in this direction has been carried out, for example, by Otto [18] in CO_2-LBW of steel. In his study, the plasma intensity signal emitted during the welding process was measured over time and subsequently analyzed to determine the predominant frequency of the plasma emission. The laser power was then modulated at this frequency (resonant stimulation), which lead to the stabilization of the penetration depth of the weld bead. This temporal beam shaping approach was based on the idea that energy can be supplied very efficiently to an oscillating system by exciting it at its resonant frequency. If an overall system consists of several coupled subsystems, it can be influenced by external periodic excitation so that it performs stable oscillations at the resonant frequency of one of its subsystems. As described in [18], the advantage of this method is that a system with chaotic behavior can be transformed into a system with periodic dynamics without the need for feedback of the system dynamics. Stabilization of the welding process is therefore possible without the use of a closed control

loop. In the case of the specific welding process analyzed in this study, it is still unclear which subsystem and which frequencies are most relevant, and this remains a topic of ongoing research. Determining this is particularly challenging because each system is unique and lacks a standard reference. For example, two systems with different shape durations will vibrate at different eigenfrequencies, even if all other process parameters are identical. The goal is to identify the relevant welding subprocess and its time scale, so that the desired welding outcome can be achieved by stimulating this subprocess at the proper frequency.

CONCLUSIONS

Although the tested duration times for the selected shape sequencing configuration produced unsatisfactory welds, the key outcome of this work is the demonstration that precise excitation of the keyhole surface can be achieved through dynamic beam shaping by simply adjusting one of the shaping parameters. In this regard, high-fidelity numerical modeling enabled the visualization and analysis of particular aspects of the process that may be beyond the reach of experimental setups. The important insights of this study are summarized below:

1. Different beam shapes and shaping strategies induce different vibration modes in the keyhole, so each configuration should be assessed according to its particular vibration characteristics.
2. Sequencing two shapes that are symmetrical about the process mid-plane, as performed in this work, induces a pulsed excitation transverse to the feed direction on the keyhole surface, with the pulse width determined by the shape durations.
3. The pulsed signal is subsequently transmitted to the melt pool, influencing its behavior. Certain shape durations favor a more or less effective excitation of the melt pool.

This work provides just one example of the many beam shaping configurations that can be analyzed through simulation. Future work will focus on examining other shaping parameters and strategies.

ACKNOWLEDGEMENTS

All experimental results, beam shape generation tool, and descriptions of the beam shapes used in the numerical implementation were provided by Civan Advanced Technologies ltd. The authors gratefully acknowledge Nina Armon, Rachel Assa, Udi Greenberg, Rami Cohen, Tom Shalev, and Ami Spira for their contributions and valuable discussions.

APPENDIX I

Table A1 Material properties of EN AW-5083: **solid state**

Property	T (K)	Value	Unit	Ref.
density ρ	300	2660	kg m^{-3}	[19]
	773	2556	kg m^{-3}	[19]
	873	2510	kg m^{-3}	[19]
bulk modulus K	300	$75.2 \cdot 10^9$	kg s^{-2} m^{-1}	[20]
specific heat capacity c_p	300	900	m^2 s^{-2} K^{-1}	[19]
	873	1224	m^2 s^{-2} K^{-1}	[19]
thermal conductivity λ	300	120	kg m s^{-3} K^{-1}	[19]
	873	164	kg m s^{-3} K^{-1}	[19]
surface energy σ	300	0.64	kg s^{-2}	[21]
refractive index n	300	0.97	-	†
	858	2.82	-	†
extinction coefficient κ	300	10.6	-	†
	858	10.6	-	†

† Assumed value based on the absorptivity at ~1 μm wavelength reported in [22].

Table A2 Material properties of EN AW-5083: **liquid state**

Property	T (K)	Value	Unit	Ref.
density ρ	950	2386	kg m^{-3}	[23]
	1650	2177	kg m^{-3}	[23]
	2790	2040	kg m^{-3}	[22]
bulk modulus K	933	$38.0 \cdot 10^9$	kg s^{-2} m^{-1}	[24]
	2400	$14.0 \cdot 10^9$	kg s^{-2} m^{-1}	[24]
kinematic viscosity ν	864	$6.10 \cdot 10^{-7}$	m^2 s^{-1}	[25]
	1000	$4.57 \cdot 10^{-7}$	m^2 s^{-1}	[25]
	1600	$2.30 \cdot 10^{-7}$	m^2 s^{-1}	[25]
	2793	$1.41 \cdot 10^{-7}$	m^2 s^{-1}	[25]
specific heat capacity c_p	933	1127	m^2 s^{-2} K^{-1}	[23]
thermal conductivity λ	933	89.3	kg m s^{-3} K^{-1}	[23]
	1500	105.1	kg m s^{-3} K^{-1}	[23]
	2000	112.7	kg m s^{-3} K^{-1}	[26]
	2600	115.1	kg m s^{-3} K^{-1}	[26]
surface energy σ	933	0.87	kg s^{-2}	[26]
	1550	0.80	kg s^{-2}	[26]
refractive index n	933	6.65	-	†
	2793	6.65	-	†
extinction coefficient κ	933	10.6	-	†
	2793	7.15	-	†

† Assumed value based on the absorptivity at ~1 μm wavelength reported in [22].

Table A3 Material properties of EN AW-5083: **vapor state**

Property	T (K)	Value	Unit	Ref.
density ρ	-	*ideal gas law*		
bulk modulus K	-	$1 \cdot 10^5$	kg s^{-2} m^{-1}	
kinematic viscosity ν	-	*ideal gas law*		
specific heat capacity c_p	2800	770	m^2 s^{-2} K^{-1}	[27]
	6000	845	m^2 s^{-2} K^{-1}	[27]
thermal conductivity λ	3000	0.15	kg m s^{-3} K^{-1}	
	5000	0.24	kg m s^{-3} K^{-1}	
surface energy σ	-	0	kg s^{-2}	
refractive index n	-	1	-	
extinction coefficient κ	-	0	-	

Table A4 Material properties of EN AW-5083: **state-independent properties**

Property	T (K)	Value	Unit	Ref.
molar mass M	-	$26.98 \cdot 10^{-3}$	kg mol^{-1}	[28]
solidus $T_{solidus}$	-	864	K	[19]
liquidus $T_{liquidus}$	-	911	K	[19]
boiling temperature $T_{boiling}$	-	2793	K	[28]
latent heat of fusion L_{fusion}	-	$394.3 \cdot 10^3$	m^2 s^{-2}	[29]
latent heat of vaporization $L_{vaporization}$	-	$1.09 \cdot 10^7$	m^2 s^{-2}	[28]

Table A5 Material properties of air

Property	T (K)	Value	Unit	Ref.
molar mass M	-	$28.014 \cdot 10^{-3}$	kg mol^{-1}	
density ρ	-	*ideal gas law*		
bulk modulus K	-	$1 \cdot 10^5$	kg s^{-2} m^{-1}	
kinematic viscosity ν	-	*kinetic theory*		
		$\nu_0 = 1.593 \cdot 10^{-5}$	m^2 s^{-1}	[27]
		$\rho_0 = 1.1233$	kg m^{-3}	[27]
		$T_0 = 300$	K	
specific heat capacity c_p	300	1041.3	m^2 s^{-2} K^{-1}	[27]
	1800	1270.8	m^2 s^{-2} K^{-1}	[27]
thermal conductivity λ	300	$2.597 \cdot 10^{-2}$	kg m s^{-3} K^{-1}	[27]
	900	$6.052 \cdot 10^{-2}$	kg m s^{-3} K^{-1}	[27]
	1800	$10.088 \cdot 10^{-2}$	kg m s^{-3} K^{-1}	[27]
surface energy σ	-	0	kg s^{-2}	
refractive index n	-	1	-	
extinction coefficient κ	-	0	-	

References

[1] M. SCHMIDT, K. CVECEK, J. DUFLOU, F. VOLLERTSEN, C. B. ARNOLD, M. J. MATTHEWS: 'Dynamic beam shaping–Improving laser materials processing via feature synchronous energy coupling', *CIRP Annals*, Vol. 73, No. 2, pp. 533-559, 2024, doi: https://doi.org/10.1016/j.cirp.2024.05.005.

[2] E. SHEKEL, Y. VIDNE, B. URBACH: '16kW single mode CW laser with dynamic beam for material processing', *Proc. SPIE 11260, Fiber Lasers XVII: Technology and Systems*, 1126021, 2020, doi: https://doi.org/10.1117/12.2545900.

[3] R. WEBER, J. WAGNER, A. PETER, C. HAGENLOCHER, A. SPIRA, B. URBACH, E. SHEKEL E, Y. VIDNE: 'Basic Properties of High-Dynamic Beam Shaping with Coherent Combining of High-Power Laser Beams for Materials Processing', *Journal of Manufacturing and Materials Processing*, 9, 85, 2025, doi: https://doi.org/10.3390/jmmp9030085.

[4] D. DITTRICH, S. BÖRNER, J. BARRIOS LARRAÑAGA, T. SAHM, A. JAHN, A. WETZIG: 'Coherent beam combining - Beam characterization of a new 14 kW CBC laser source and first results on copper welding', *Procedia CIRP*, Vol. 124, pp. 724-729, 2024, doi: https://doi.org/10.1016/j.procir.2024.08.211.

[5] M. SAWANNIA, J. WAGNER, P. STRITT, R. RAMSAYER, C. HAGENLOCHER, T. GRAF: 'Response of the melt pool and vapour capillary on dynamic beam shaping in the kHz regime during laser welding', *Procedia CIRP*, Vol. 124, pp. 430-433, 2024, doi: https://doi.org/10.1016/j.procir.2024.08.147.

[6] C. PRIETO, E. VAAMONDE, D. DIEGO-VALLEJO, J. JIMENEZ, B. URBACH, Y. VIDNE, E. SHEKEL: 'Dynamic laser beam shaping for laser aluminium welding in e-mobility applications', *Procedia CIRP*, Vol. 94, pp. 596-600, 2020, doi: https://doi.org/10.1016/j.procir.2020.09.084.

[7] S. OLSCHOK, M. TROISE, U. REISGEN: 'Laser beam welding of high thickness sheet metal with highly dynamic beam shaping', *Procedia CIRP*, Vol. 124, pp. 733-736, 2024, doi: https://doi.org/10.1016/j.procir.2024.08.213.

[8] C. ZENZ, M. BUTTAZZONI, T. FLORIAN, K. E. CRESPO ARMIJOS, R. GÓMEZ VÁZQUEZ, G. LIEDL, A. OTTO: 'A compressible multiphase Mass-of-Fluid model for the simulation of laser-based manufacturing processes', *Computers & Fluids*, Vol. 268, 106109, 2024, doi: https://doi.org/10.1016/j.compfluid.2023.106109.

[9] C.-R. SONG, B.-X. DONG, S.-Y. ZHANG, H.-Y. YANG, L. LIU, J. KANG, ET AL.: 'Recent progress of Al–Mg alloys: Forming and preparation process, microstructure manipulation and application', *Journal of Materials Research and Technology*, Vol. 31, pp. 3255-3286, 2024, doi: https://doi.org/10.1016/j.jmrt.2024.07.051.

[10] J. HAN, Y. SHI, G. ZHANG, V. KORZHYK, W.-Y. LE: 'Minimizing defects and controlling the morphology of laser welded aluminum alloys using power modulation-based laser beam oscillation', *Journal of Manufacturing Processes*, Vol. 83, pp. 49-59, 2022, doi: https://doi.org/10.1016/j.jmapro.2022.08.031.

[11] H. G. WELLER, G. TABOR, H. JASAK, C. FUREBY: 'A tensorial approach to computational continuum mechanics using object-oriented techniques', *Comput. Phys.*, Vol. 12 (6), pp. 620-631, doi: https://doi.org/10.1063/1.168744.

[12] A. OTTO, H. KOCH, R. GÓMEZ VÁZQUEZ: 'Multiphysical Simulation of Laser Material Processing', *Physics Procedia*, Vol. 39, pp. 843-852, https://doi.org/10.1016/j.phpro.2012.10.109.

[13] A. OTTO, H. KOCH, K.-H. LEITZ, M. SCHMIDT: 'Numerical Simulations - A Versatile Approach for Better Understanding Dynamics in Laser Material Processing', *Physics Procedia*, Vol. 12 (A), pp. 11-20, 2011, doi: https://doi.org/10.1016/j.phpro.2011.03.003.

[14] A. OTTO, M. BUTTAZZONI, C. DURÁN, T. FLORIAN, C. ZENZ: *Universal Numerical Simulation Model for Laser Material Processing', preprint, 2026, accepted for publication in 'Scaling of*

Laser Processing – Making Light Matter, J. BONSE, A. F. LAGSANI (EDS.), Springer, Cham, Switzerland. Preprint available at: https://doi.org/10.48550/arXiv.2509.22666. The final authenticated version will be available online in the Springer Series in Optical Sciences: https://link.springer.com/book/9783032171320.

[15] C. ZENZ, P. S. COOK, L. VÖRÖS, A. OTTO: 'A critical comparison of one- and two-fluid approaches for the simulation of laser-induced melt pool formation and vaporisation', *Discover Materials*, Vol. 5, 266, 2025, doi: https://doi.org/10.1007/s43939-025-00434-0.

[16] O. BOCKSROCKER, N. SPEKER, M. BERANEK, T. HESSE: 'Reduction of spatters and pores in laser welding of copper hairpins using two superimposed laser beams', *Proc LIM*, pp. 1-8, 2019.

[17] P. WELCH: 'The use of fast Fourier transform for the estimation of power spectra: A method based on time averaging over short, modified periodograms', *IEEE Transactions on Audio and Electroacoustics*, Vol. 15 (2), pp. 70-73, 1967, doi: https://doi.org/10.1109/TAU.1967.1161901.

[18] A. OTTO: 'Transiente Prozesse beim Laserstrahlschweißen', Doctoral dissertation, Friedrich-Alexander-Universität Erlangen-Nürnberg, 1997.

[19] Z. JIANG, X. HUA, L. HUANG ET AL.: 'Effect of multiple thermal cycles on metallurgical and mechanical properties during multi-pass gas metal arc welding of Al 5083 alloy', *Int. J. Adv. Manuf. Technol.*, Vol. 93, pp. 3799-3811, 2017, doi: https://doi.org/10.1007/s00170-017-0771-6.

[20] S. RAJU, K. SIVASUBRAMANIAN, E. MOHANDAS: 'The high temperature bulk modulus of aluminium: an assessment using experimental enthalpy and thermal expansion data', *Solid State Communications*, Vol. 122 (12), pp. 671-676, 2002, doi: https://doi.org/10.1016/S0038-1098(01)00517-8.

[21] P.-F. PARADIS, T. ISHIKAWA: 'Surface Tension and Viscosity Measurements of Liquid and Undercooled Alumina by Containerless Techniques', *Jpn. J. Appl. Phys.*, Vol. 44, 5082, 2005, doi: https://dx.doi.org/10.1143/JJAP.44.5082.

[22] D. MARLA ET AL.: 'Models for predicting temperature dependence of material properties of aluminum', *J. Phys. D: Appl. Phys.*, Vol. 47 (10), 105306, doi: http://dx.doi.org/10.1088/0022-3727/47/10/105306.

[23] M. LEITNER, T. LEITNER, A. SCHMON ET AL.: 'Thermophysical Properties of Liquid Aluminum', *Mater. Trans. A*, Vol. 48, pp. 3036-3045, 2017, doi: https://doi.org/10.1007/s11661-017-4053-6.

[24] R.N. SINGH, S. ARAFIN, A.K. GEORGE: 'Temperature-dependent thermo-elastic properties of s-, p- and d-block liquid metals', *Physica B: Condensed Matter*, Vol. 387 (1-2), pp. 344-351, 2007, doi: https://doi.org/10.1016/j.physb.2006.04.029.

[25] A. T. DINSDALE, P. N. QUESTED: 'The viscosity of aluminium and its alloys--A review of data and models', *J. Mater. Sci.*, Vol. 39, pp. 7221-7228, 2004, doi: https://doi.org/10.1023/B:JMSC.0000048735.50256.96.

[26] A. V. GUSAROV, I. SMUROV: 'Thermal model of nanosecond pulsed laser ablation: Analysis of energy and mass transfer', *J. Appl. Phys*, Vol. 97 (1), 014307, doi: https://doi.org/10.1063/1.1827321.

[27] E. W. LEMMON, I. H. BELL, M. L. HUBER, M. O. MCLINDEN: 'Thermophysical properties of fluid systems', in: Linstrom, P.J. and Mallard, W.G. (eds.) NIST Chemistry WebBook, *NIST Standard Reference Database 69*, National Institute of Standards and Technology, http://dx.doi.org/10.18434/T4D303.

[28] M. TIRYAKIOĞLU, A. E. MAYER: 'On estimating the intrinsic surface tension of liquid aluminum and its temperature coefficient', *J. Mater. Sci.*, Vol. 59, pp. 12781-12792, 2021, doi: https://doi.org/10.1007/s10853-024-09909-6.

[29] A. E. W. JARFORS, P. JANSSON: 'Selecting Cast Alloy Alloying Elements Suitable for a Circular Society', *Sustainability*, Vol. 14, 6584, 2022, doi: https://doi.org/10.3390/su14116584.